



NRL/MR/7540--06-8870

# Aerosol Optical Depth Analysis with NOAA GOES and POES in the Western Atlantic

ARUNAS P. KUCIAUSKAS

*Meteorological Applications Development Branch  
Marine Meteorology Division*

PHILIP A. DURKEE

*Department of Meteorology  
Naval Postgraduate School  
Monterey, CA*

DOUGLAS L. WESTPHAL

*Atmospheric Dynamics and Prediction Branch  
Marine Meteorology Division*

February 17, 2006



## CONTENTS

1. Introduction .....	1
2. Satellite Aerosol Optical Depth Retrieval Method.....	3
3. Data and Methodology .....	5
3.1 NOAA Polar Orbiting Environmental Satellite Advanced Very High Resolution Radiometer (AVHRR) .....	5
3.2 NOAA Geostationary Orbiting Environmental Satellite (GOES-8) Imager.....	6
3.3 AERONET Sun-sky Scanning Spectral Radiometer .....	6
4. GOES-8 Calibration and Correction Processes.....	7
5. Results .....	9
5.1 A Case Study of High AOD Conditions.....	10
5.2 Results from 22 Cases.....	12
6. Conclusions .....	16
List of References .....	19

# Aerosol Optical Depth Analysis with NOAA GOES and POES in the Western Atlantic

## 1. Introduction

Monitoring tropospheric aerosols on a global scale is essential for evaluating the earth's radiation budget. Aerosols impact the radiation process partly by scattering incident solar radiation back to space and by interacting with clouds in a way that increases overall albedo (Charlson *et al.*, 1992, Twomey *et al.*, 1977, IPCC, 1996). King *et al.* (1999) reports the impact of aerosol radiative forcing, both directly (scattering) and indirectly (interaction with clouds), produces a cooling range of  $-1.4 \pm 1.5 \text{ W m}^{-2}$  to  $-2.5 \pm 2 \text{ W m}^{-2}$ . This result offsets the well-known concept of the greenhouse warming impact, estimated to be  $+2.5 \pm 0.3 \text{ W m}^{-2}$ .

Another research area of global aerosol impact focuses on the transport of dust and pollutants from one region to another. ACE-Asia (Huebert, *et al.*, 2003) was a 4-year project (2001 – 2004) devoted to the study of aerosol profiles in the Pacific basin generated by desert dust and industrial pollution over Asia. The Puerto Rico Dust Experiment (PRIDE) in 2000 (Reid, *et al.*, 2002) studied the impacts of African desert dust that is transported over to the Caribbean and the eastern U.S.

Given the challenges listed above, there is a developing interest to globally quantify aerosol properties on fine spatial and temporal scales. Thus far, this analysis has proven to be a daunting task, since most established aerosol sensing is land-based, providing poor spatial and temporal coverage. Higurashi *et al.* (1999) suggests that aerosol concentration, size distribution, composition, and optical properties will have to be measured globally, and that satellite remote sensing is an effective tool for such a task. Over the past few decades, scientists have developed algorithms to convert satellite upwelling radiances into aerosol properties such as optical depth. So far, most of the

aerosol remote sensing studies have used the Polar Orbiting Environment Satellite (POES) National Oceanographic and Atmospheric Administration (NOAA) Advanced Very High Resolution Radiometer (AVHRR) sensor channel 1 and 2 data. Table 1 provides the channel characteristics for the AVHRR sensor. These algorithms were developed by assuming certain aerosol characteristics such as scattering phase function and single scatter albedo before processing the upwelling radiances (Durkee *et al.* 2000, Durkee *et al.* 1991, Kaufman *et al.* 1990, Higurashi and Nakajima, 1999).

This study focuses on one such algorithm developed by Durkee *et al.* (1990) and Durkee *et al.* (1999) (hereafter referred to as the NPS algorithm). The NPS algorithm ingests AVHRR data within a cloud-free, single scatter environment. The scattering phase function was parameterized based on the ratio of channel 1 and 2 radiances; a necessary step in solving the radiative transfer problem. During three recent field campaigns, Durkee *et al.* (2000) has shown that the NPS algorithm performs well for aerosol optical depths (AOD) below 0.4 at 0.63  $\mu\text{m}$  wavelength. But the results only provided once or twice-daily snapshots of AOD over experimental regions, since the polar orbiting AVHRR sensor passes over non-polar regions a few times per day<sup>1</sup>. For this study, the NPS algorithm has been adapted to estimate AOD using GOES visible data. Table 2 provides channel characteristics for the GOES GVAR sensor. Since the GOES data contains only 1 visible channel, an estimate of the aerosol size distribution is not directly made available to GOES AOD processing. Instead, the aerosol information obtained from each pixel within the NOAA AVHRR AOD processing is passed into the

---

<sup>1</sup> This statement applies over mid-latitude and tropical regions since passes converge over the poles, resulting in decreasing frequency toward the equator.

GOES AOD processing. A more elaborate description of this process can be found in Brown (1997) and Kuciauskas (2002).

The focus of this article is to evaluate the algorithm over open water regions near islands in the western Atlantic Ocean. The following issues will be addressed:

- Proper radiance calibration of the visible sensor on GOES platforms
- Validation of the AOD derived from the retrieval algorithm using AERONET estimates over the Caribbean and eastern Atlantic Ocean
- Evaluation of the phase function parameters used in the retrieval algorithm

Section 2 describes the radiative transfer theory and the simplifying atmospheric assumptions used in the satellite optical depth retrievals. Section 3 describes the data sets and basic instrumentation used. Section 4 describes the calibration and correction techniques applied to the retrieved GOES channel 1 radiance. Section 5 discusses the results and Section 6 presents the conclusions.

## 2. Satellite Aerosol Optical Depth Retrieval Method

For the aerosol optical depth environment, Brown (1997) and Durkee *et al.* (1991) simplify the general form of the radiative transfer equation by applying the following assumptions: the AVHRR visible instrument senses aerosol particles within a cloud-free, marine environment, with a single scatter approximation. In addition, contributions from ozone absorption, Rayleigh and ocean surface effects are estimated and eliminated from the calculation. The equation is then reduced to a linear relationship between satellite-sensed radiances due to aerosol particles and aerosol optical depth:

$$L_a = \frac{\omega_o F_o}{4\mu} p(\Psi_s) \delta_a \quad (1)$$

where:

$L_a$  = diffuse radiance from aerosols

$\delta_a$  = optical depth of aerosols

$p(\psi_s)$  = scattering phase function

$F_o$  = incoming solar radiative flux

$\omega_o$  = single scatter albedo

$\mu$  = cosine of satellite zenith angle

To obtain radiances from only aerosol sources ( $L_a$ ), the following steps are applied. Radiances from Rayleigh scattering are removed by a calculation method according to Turner (1973). Radiances due to sun glint contamination are extracted by visually discerning sun glint patterns from AVHRR visible and near IR images. The elimination of radiances over cloudy pixels and from sources other than aerosols are described in Durkee *et al.* (1999).

The single scatter albedo ( $\omega_o$ ) is a measure of the ratio of radiance scattered versus radiance absorbed. For marine aerosols sensed by visible wavelengths, the particles (salt and sulfate) are weakly absorbing and therefore, the single scatter albedo ( $\omega_o$ ) is assumed to be one. This assumption holds for the smaller aerosol particles. During episodes with large dust particles, absorption becomes more significant, resulting in  $\omega_o$  values less than one. By assuming  $\omega_o = 1$ , the NPS algorithm underestimates AOD for absorbing aerosols. The incoming solar radiance ( $F_o$ ) is a known constant. The cosine of the satellite zenith angle ( $\mu$ ) is obtained by the satellite-earth geometry. Aerosol optical depth ( $\delta_a$ ) is expressed as the sum of the atmospheric extinction integrated vertically from the surface through the atmosphere. The single scatter phase function  $p(\psi_s)$  determines which direction the radiation is scattered when it encounters an

aerosol particle. Determining  $p(\psi_s)$  requires knowledge of the aerosol composition and size distribution, which are not routinely available. Therefore,  $p(\psi_s)$  must be parameterized. Durkee *et al.* (1991), Brown (1997) and Durkee *et al.* (1999) developed the parameterization technique for the NPS algorithm of using the ratio of the channel 1 (visible) and channel 2 (near-IR) data for each NOAA AVHRR pixel to select one of 7 models of maritime aerosol size distributions, ranging from pristine to dusty conditions and then estimating the phase function values using a lookup table and the viewing geometry. Previous applications of this method may be found in Brown (1997), Smith (1998), Durkee *et al.* (1999) and Kuciauskas (2002).

As mentioned in the previous section, the aerosol size distribution information is passed from each AVHRR pixel to the corresponding GOES pixel. An assumption that aerosol conditions don't appreciably change between the NOAA AVHRR and GOES times is applied.

### **3. Data and Methodology**

To validate the optical depth retrieval method, a case study approach was developed wherein cases were selected based on the availability of collocated and concurrent data from NOAA POES and GOES, and AERONET ground-based radiometers. This section describes the datasets and methods used for this study.

#### **3.1. NOAA Polar Orbiting Environmental Satellite Advanced Very High Resolution Radiometer (AVHRR)**

The AVHRR instrument senses upwelling radiances of 5 channels, ranging from the visible to the infrared. Over the experimental region, the NOAA-16 AVHRR provided the local afternoon data (~1800 UTC) while the NOAA-14 AVHRR provided

data late in the afternoon (~2100 UTC). The data from the NOAA-14 was at times degraded due to low sun angle problems. Therefore, the NOAA-16 data was considered the more reliable dataset. All AVHRR channels are calibrated prior to launch. Channels 1 and 2 have no onboard calibration systems. Post calibration methods for these channels were developed by the NOAA/NESDIS Office of Research Applications, based on results of Rao and Chen (1995) and Rao *et al.* (1999).

The visible channel 1 data, centered at 0.63  $\mu\text{m}$ , is used in the AOD calculations. Channel 1 and the near-IR channel 2 data (centered at 0.86  $\mu\text{m}$ ) are used to select the aerosol model, as mentioned in section 2.1.

### **3.2. NOAA Geostationary Orbiting Environmental Satellite (GOES-8) Imager**

The GOES-8 imager is onboard the Geosynchronous Operational Environmental Satellite (GOES) series of satellites and covers the western Atlantic region. The GOES imager scans in 5 channels: channel 1 in visible, channels 2 – 5 in IR. For this study, channel 1 (central wavelength ~0.65  $\mu\text{m}$ ) is used in the AOD calculations. Like the NOAA AVHRR, the visible channel does not have an onboard calibration system. Immediately after the launch, there was a nonlinear decrease in signal strength within the GOES-8 imager. Furthermore, the GOES imager is much noisier than the AVHRR sensor. For this study, the visible radiances were adjusted in order to be comparable to the AVHRR visible radiances. Section 4 describes these correction procedures.

### **3.3. AERONET Sun-sky Scanning Spectral Radiometer**

Data collected from the AERONET automated radiometers are used as the ground truth AOD for this study. AERONET consists of a global network of ground-based automated CIMEL Electroniques 318A spectral radiometers that make direct sun or sky

measurements. The direct sun measurements are made in 8 spectral bands centered at 0.34, 0.38, 0.44, 0.50, 0.67, 0.87, 0.94, and 1.02  $\mu\text{m}$ . The 0.67  $\mu\text{m}$  wavelength data is comparable to that used in the optical depth calculation from both the GOES and NOAA retrievals and is used in the comparison. Under cloud free conditions, the AOD uncertainty at 0.67  $\mu\text{m}$  is less than  $\pm 0.01$ . Detailed information about the operations and instruments of the AERONET system is provided in Holben *et al.* (1998).

AERONET data was obtained from instruments installed on three island sites: eastern Bermuda, (U.K.) ( $32^{\circ} 22' \text{N}$ ,  $64^{\circ} 41' \text{W}$ ), La Paguera, Puerto Rico ( $17^{\circ} 58' \text{N}$ ,  $67^{\circ} 02' \text{W}$ ) and Guadaloup, Island (Fr.) ( $16^{\circ} 19' \text{N}$ ,  $61^{\circ} 30' \text{W}$ ), all within the western Atlantic Basin (see Figure 1). For all 3 sites, the dataset contains only the times that have not been contaminated by clouds. Cloud events were flagged as missing data within the AERONET measurements.

#### **4. GOES-8 Calibration and Correction Processes**

Compared to the AVHRR, calibrating the GOES-8 channel 1 radiances was significantly more challenging, resulting in less accurate data. There have been several attempts to perform vicarious calibration techniques to adjust for the weakening signal strength and to take into account the post-launch degradation. There is an additional problem with noise and the signal radiometric resolution, inherent within the GOES sensors. Figure 2 displays an example of radiance comparisons between the calibrated GOES and AVHRR datasets. The image passes occurred at a similar time and were registered over the same 100 km by 100 km domain surrounding Bermuda. In addition, both satellites had similar viewing geometries (scatter angles were  $\pm 0.1^{\circ}$  of each other). The atmospheric conditions immediately south of Bermuda (outlined in red) were clear

and homogeneous at this time. The right side panels within Figure 2 are plots of the histogram frequency distribution of radiances that were extracted within the outlined region. As expected, the NOAA-16 image in Figure 2(b) displays a relatively homogeneous field of radiances. Its corresponding frequency histogram shows a pronounced signal peak with a narrow radiometric width, indicative of the pristine atmospheric conditions. In contrast, the GOES-8 sensor, situated in an orbit that is 40 times the distance of the NOAA sensor, produces an image (shown in Figure 2(a)) that is significantly noisier. Its corresponding histogram displays a weaker signal peak and wider radiometric range. As atmospheric conditions become hazier, the GOES-8 peak signal and radiometric resolutions become even less discernable, thus reducing the confidence level of processed AOD calculations. In addition, the GOES-8 signal peak of  $\sim 16 \text{ Wm}^{-2}\text{sr}^{-1}\mu\text{m}^{-1}$  is significantly weaker than the NOAA-16 signal peak of  $\sim 22.5 \text{ Wm}^{-2}\text{sr}^{-1}\mu\text{m}^{-1}$ , thus necessitating a further correction factor to GOES-8 before further processing.

To match GOES with NOAA data during AOD processing, two correction techniques were applied to the GOES channel 1 radiance data. Rao and Zhang (1999) and Rao *et al.* (1999) developed a calibration methodology of GOES-8 channel radiance by a vicarious technique, selecting a radiometrically stable calibration site located in the Sonoran desert (34.0°N/114.1°W). Radiometrically stable calibration is defined as the long term mean albedo at the top of the atmosphere remaining uniform in time.

The gain factor determined by Rao (1999) increases with time, corresponding to the weakening signal within the GOES-8 channel 1 sensor. For this report, the gain factor ranged from 1.727 during the earliest case (27 July) to 1.740 during the latest case

(29 September). A preliminary assessment of the calibrated GOES data indicated that its resulting AOD values were significantly higher than the NOAA-generated AOD as well as the AERONET observations of AOD. Therefore, a further correction method was applied based on comparisons between GOES-8 and NOAA-16 channel 1 radiances, whose wavelengths, centered on 0.65 and 0.63  $\mu\text{m}$ , respectively, were similar. The calibrated AVHRR channel 1 radiances are assumed to be accurate. The process involved the collection of a sample of cases when the GOES and NOAA viewing geometries over a selected location were similar. GOES and NOAA viewing geometries were defined as 'similar' when the scatter and azimuth angles were within  $\pm 0.1^\circ$  of each other. Figure 3 presents the comparisons of over 296 pairs of GOES and NOAA channel 1 radiances. As shown, only the radiances along the low end of the radiance spectrum were plotted; it is at this range ( $\leq 40 \text{ Wm}^{-2}\text{sr}^{-1}\mu\text{m}^{-1}$ ) where detection of aerosols would occur. The orange shade indicates the region where there was much overlap among data pairs. As shown, there was very poor correlation between the NOAA and GOES data due to the large noise problem in GOES. A correction consistent with offset of  $5.5 \text{ Wm}^{-2}\text{sr}^{-1}\mu\text{m}^{-1}$  (shown in Figure 3) was applied to GOES-8 data. Applying this correction produced results comparable to the NOAA dataset.

## 5. Results

To evaluate the performance of the NPS algorithm, a case study approach over the three island regions was conducted over 22 days in July and September of 2001. The following section describes one such case. Section 5.2 summarizes the evaluation of the algorithm for all 22 cases.

## **5.1. A Case Study of High AOD Conditions**

### **5.1.1. Synoptic Discussion**

During the summer months, dust generated from the African deserts is often transported across the southern latitudes of the Atlantic Ocean basin by the easterly trade winds, thereby impacting the visibility and aerosol characteristics over regions of the Caribbean and the east coast of the US (Chiapello, *et al.*, 1999 and Prospero, 1999). For this case, the SeaWiFs image in Figure 4 displays a dust plume approaching the island of Guadeloupe on 17 September. The dust plume crossed over Guadeloupe a day later on 18 September (not shown).

The dust transport was also predicted by the Naval Research Laboratory's Aerosol Analysis and Prediction System (NAAPS) (Westphal, 2003 and Westphal, [<http://www.nrlmry.navy.mil/aerosol>]). Figure 5 shows the leading edge of a significant dust plume reaching Guadeloupe on 18 September at 18:00 UTC. Contours of heavy concentrations of dust are imbedded within this plume. The 850 mb wind pattern at 18:00 UTC supports the continuing transport of the dust plume over the Guadeloupe and Caribbean regions.

The GOES-8 image in Figure 6 provides another view of the large region of dust aerosols surrounding the Guadeloupe Island region (inside the annotated box) around local noon on 18 September at 17:15 UTC (12:15 LST). The large cloud mass just to the north of Guadeloupe Island region eventually moved south over the study region, and contaminated some of the AOD measurements later in the day.

### 5.1.2. AOD and Phase Function Analysis

Figure 7 presents AOD images from GOES-08 and NOAA-16 data. As mentioned in Section 2, the NOAA AOD processing supplies the aerosol size distribution parameters to the GOES AOD processing. For this case study, the NOAA-16 data at 17:50 UTC supplied these aerosol parameters to GOES-08 data every  $\frac{1}{2}$  hr between 16:45 UTC and 20:45 UTC. Only the GOES image at 17:45 UTC image is shown in Figure 6. Within Figure 6, a small red box (approximately 15 X 15 km) is annotated for each image to show the area where the representative AOD value was extracted for that time. This value was then compared to the sampled AOD of the nearby AERONET site (indicated by a red dot). Determining the representative AOD value from the NOAA-16-generated AOD field was relatively easy because there were little or no variations within the red box. In contrast, obtaining the representative AOD from the noisy GOES-generated AOD field was oftentimes far more difficult, especially during the later times during the study period. Therefore, a technique to standardize the extraction of the representative AOD from both AVHRR and GOES data was developed and is described next.

An example of the AOD extraction process is displayed in Figure 8. The histogram frequency plot was generated from within the red box in the 17:45 UTC panel in Figure 6. First, a solid red curve was manually drawn, representing the approximating curve of the frequency distribution of AOD. Next, the peak of the distribution was identified and translated to an AOD value of  $\sim 0.44$ . An estimate of the variability of AOD was then determined by locating the half-amplitude of the curve, on either side of the peak (blue arrows). In this case, the variability about the AOD estimate was

approximately  $-0.10$  and  $+0.10$ . Depending on visibility and cloud conditions, the variability of GOES-generated AOD can exceed  $\pm 0.50$  on either side of the AOD estimate. In contrast, the variability for AVHRR-generated AOD rarely exceeds  $\pm 0.01$ .

Figure 9 presents the time series of AOD for this case. Both the GOES-derived AOD and the AERONET observations of AOD are in good agreement, with high AOD values throughout the time period. Cloud contamination resulted in time gaps of AOD measurements between 19:15 UTC and 20:15 UTC. The lengths of the variability bars associated with GOES-8 data increase with time. The AOD generated from the NOAA-16 data at 17:50 UTC (AOD  $\sim 0.45$ ) and the NOAA-14 data at 21:17 UTC (AOD  $\sim 0.48$ ) are also in agreement with AERONET observations.

Figure 10 displays comparisons of the inferred phase function values between the NPS algorithm's AOD calculations and the AERONET AOD observations. The NPS algorithm-derived phase function values are obtained from the processing of the ratio of channel 1 and 2 radiances in the POES data, as described in Section 2. The AERONET-derived phase function values are calculated using Equation 1, where the input parameters consist of the AERONET AOD and the remaining variables supplied by the POES parameters. As shown, all values are within the backscatter portion ( $90^\circ - 180^\circ$ ). Figure 10 suggests that the NPS algorithm may be overestimating  $p(\psi_s)$  at scattering angles near  $180^\circ$ .

## **5.2. Results from 22 Cases**

### **5.2.1. Overview**

Table 3 lists the dates, times and locations of all of the cases in this study. The selected data was based on the availability of both satellite and AERONET data. The

common occurrence of sun glint within NOAA POES data caused the elimination of a number of potential case examples. Seven cases are designated as a dusty environment, with AOD values greater than 0.25. Unfortunately, data for the analysis of these cases was limited because of a greater tendency toward more cloud contamination surrounding all 3 islands within the study.

For each case, AERONET AOD was compared with the nearest satellite AOD without land or cloud contamination. Figure 11 presents the measurement distances between the satellite-derived AOD and the AERONET observations. The most favorable region for comparison was Bermuda, with an average separation of only 19 km. The islands of Guadeloupe and Puerto Rico contain topography that often produces orographically enhanced cloud cover on a daily basis. To avoid cloud contamination, there were several instances where separation distances were as large as 80 km. The comparisons were still made at the distant locations, so long as an AOD value could be retrieved.

### **5.2.2. Evaluation of the NPS algorithm**

Figure 12 compares satellite-derived AOD data with AERONET observations for all 22 cases. Within low AOD conditions ( $\delta_a < 0.25$ ), there is a slight bias for NOAA-derived AOD values toward higher values while the GOES-derived values have a slight bias toward lower AOD values. Within optically thick dust conditions ( $\delta_a > 0.25$ ), there is a tendency for the NPS algorithm to underestimate AOD. Similar findings by Smith (1998) attributed the probable cause to the “no absorption” assumption ( $\omega_0 = 1$ ) within the NPS algorithm. However, the differences shown in Figure 12 could not be eliminated, even when applying a reasonable range of  $\omega_0$  values, as provided by Kaufman

*et al.* (2001) and Reid *et al.* (2003). As shown in Figure 12, the overall standard error for AOD measurement is 0.066. For the regression analysis, the GOES and NOAA combined results in an  $R^2$  of 0.67. Individually, the NOAA regression is 0.62 while the GOES regression is higher at 0.69. Smith (1998) showed similar results when he applied the NPS algorithm to the Aerosol Characterization Experiments (ACE-1 and ACE-2), as well as the Tropospheric Aerosol Radiative Forcing Observational Experiment (TARFOX). In that study, the standard error for the NOAA POES AOD,  $0.63 \mu\text{m}$ , was 0.023, with a correlation coefficient of 0.88.

The performance of the NPS algorithm is further evaluated by the dependence of the errors on the geometry between the sun and satellite positions. Figure 13 categorizes the two regression parameters into scatter angle categories. As mentioned earlier, due to the position of the study areas and the fixed location of the GOES-8 satellite, local noon occurs around the peaks of scatter angles (total backscatter). Therefore, in Figure 13, the scatter angle category of  $170^\circ - 180^\circ$  (complete backscatter) is within the region of local noon.  $R^2$  describes the degree of correlation between satellite-derived AOD and AERONET data. For example,  $R^2 = 0.40$ , indicates that 40% of the original variability of the satellite-derived AOD can be explained, with a remaining 60% of residual variability. As shown within the bar patterns of Figure 12,  $R^2$  values are highest about  $140^\circ - 150^\circ$  ( $R^2 \sim 0.72$ ) and at  $170^\circ - 180^\circ$  ( $R^2 \sim 0.76$ ). Corresponding standard error (S.E.) values are at their lowest within the scatter angle categories of  $130^\circ - 140^\circ$  and  $170^\circ - 180^\circ$ , respectively. A possible explanation for the higher accuracy at 140 - 150 degrees could be that the selected model phase function values used within the NPS algorithm are the most accurate at these angles, as they converge toward one value at  $\sim 140$  degrees.

Therefore, there are no aerosol size distribution selection errors at this scatter angle provided the size distribution of the aerosol are well represented by the a priori models used in NPS algorithm.

Figure 14 displays the phase function analysis for the 22 cases under dusty conditions ( $\delta_a \geq 0.25$ ). Satellite-derived phase functions and the phase functions required to match the AERONET AOD are shown. Between  $140^\circ$  and  $180^\circ$ , phase function values automatically generated by the NPS algorithm indicate a pattern of higher curvature than those required to match the AERONET AOD. This result is consistent with work conducted by Collins *et al.* (2000) in the second Aerosol Characterization Experiment (ACE-2) off the west African coast. Figure 15 presents their findings. Beyond the scatter angle of  $140^\circ$ , non-spherical dust particles were observed to produce a flatter phase function shape than non-dust conditions. Figure 16 compares the 7 phase function models used in the NPS algorithm with the normalized phase function patterns supplied by Collins *et al.* (2000). Within the forward scatter angles ( $0^\circ - 90^\circ$ ), both the spherical and non-spherical contours follow the phase function patterns of the 7 models. However, within the backscatter region ( $90^\circ - 180^\circ$ ), the non-spherical phase function curve deviates from all other curves and has a flatter profile. Recent studies over the Canary Islands indicate that Saharan dust transported across the Atlantic Ocean deviates from the spherical shapes found in smaller aerosols (Maring *et al.*, 2000). Mishchenko *et al.* (1997) reports that this non-spherical effect can result in large errors in the satellite AOD calculations. As mentioned earlier, the NPS algorithm applies its theory based on non-absorbing, spherical aerosol particles. Based on Figure 16, future modifications to the

NPS algorithm warrant the incorporation of a modified phase function profile for dust conditions.

## 6. Conclusions

A radiative transfer algorithm (NPS algorithm) that estimates AOD within a cloud-free maritime atmosphere was presented for the NOAA POES and GOES imagers. This algorithm applies linearized, single-scatter theory with an estimate of bi-directional surface reflectance. Durkee *et al.* (1991) and Durkee *et al.* (2000) relate the ratio of channel 1 and 2 radiances of the AVHRR to a representative aerosol model over maritime conditions. Then, based on the viewing geometry and the assumed aerosol model, the algorithm assigns the phase function value from a lookup table. Then the GOES scheme uses the same aerosol model for the nearest pixel both in space and time. The remaining parameters used to calculate AOD are straightforward, as described in Equation 1.

Due to the unexpected post-launch degradation of signal strength, the GOES-8 visible radiance data required an additional calibration (Rao *et al.*, 1999 and Rao and Zhang, 1999). During the analysis period of this paper (July and September, 2001) signal gain factors ranging from 1.727 during the first case study (July 27, 2001) through 1.740 during the last study (September 25, 2001) were applied to the GOES raw channel 1 albedo data. In addition, preliminary comparisons of AOD between GOES and NOAA, and AERONET revealed that an additional GOES-8 channel 1 correction offset of  $-5.5\text{Wm}^{-2}\text{sr}^{-1}\mu\text{m}^{-1}$  was necessary.

To validate the NPS algorithm, retrieved AOD data was collected from 22 cases during July and September of 2001 and compared to AERONET radiometers positioned within 3 island locations of the western Atlantic Ocean. Overall, the comparison dataset

yields a correlation coefficient of 0.67 with a standard error of 0.07. Within higher AOD cases, the general trend was for the NPS algorithm to produce AOD values that underestimate AERONET-observed conditions. Attempts to vary the single scatter albedo ( $\omega_0$ ) could not explain the discrepancies. When related to scatter angles, these AOD calculations performed best within the backscatter angle ranges of 130° - 140° and 170° - 180°.

A major part of the uncertainty to the AOD processing is the proper selection of the scattering phase function. The AOD results generated from GOES data assumed that the AVHRR-determined aerosol model was unchanging throughout the entire time period, which might last as long as 8 hours. More confidence was placed on GOES-generated AOD results nearer in time to the AVHRR AOD retrieved.

Between the scatter angles of 140° through 180°, the phase function required to match the AERONET observations was flatter than that produced by the NPS algorithm. This fitted phase function profile is supported by Collins *et al.* (2000) for non-spherical dust aerosols.

Overall, the NPS AOD algorithm performed reasonably well (compared to other AOD products) as a tool in assessing global climatological parameters. The standard error values fall well within the noise range for collecting information about parameters in the earth's radiation budget studies. However, users would be greatly cautioned in applying the output from the NPS AOD algorithm toward more sensitive applications such as visibility assessments in military tactical decision aids.

**Acknowledgements.** We gratefully acknowledge the support of our research sponsors, the Oceanographer of the Navy through the program office at PEO C4I & Space PMW-

150 (PE-0603207N). We would also wish to thank the following individuals: Mr. Kurt Nielsen of NPS and Dr. Robert Wade of Science Applications International Corporation (SAIC) for their support in various satellite processing algorithms, Mr. Brent Holben and Ms. Rose Petit from AERONET for providing us with sun photometer data, Mr. Norman Kuring of NASA/Goddard Space Flight Center for providing SeaWiFs images, Dr. Jeffrey Reid from NRL for his insight into Saharan dust properties, and finally to Mr. Jeffrey Hawkins and Dr. Joseph Turk from NRL for providing us with a variety of satellite-related resources. Finally, we want to thank NRL for the time allotment and funding of this research effort through the Edison Memorial Graduate Training Program.

## LIST OF REFERENCES

- Brown, B. B., 1997: Remote measurement of aerosol optical properties using the NOAA POES AVHRR and GOES Imager during TARFOX. M.S. Thesis, Naval Postgraduate School, Monterey, CA, 73 pp.
- Charlson, R. J., S. E. Swartz, J. M. Hales, R. D. Cess, J. A. Coakley, Jr., J. E. Hansen and D. J. Hoffman, 1992: Climate forcing by anthropogenic aerosols. *Science*, **255**, 423-430.
- Chiapello, I., J. M. Prospero, J. R. Herman and N. C. Hsu, 1999: Detection of mineral dust over the North Atlantic Ocean and Africa with the Numbus 7 TOMS. *J. Geophys. Res.*, **104**, 9277-9291.
- Collins, D. R., H. H. Jonsson, J. H. Seinfeld, R. C. Flagan, S. Gassó, D. A. Hegg, P. B. Russell, B. Schmid, J. M. Livingston, E. Öström, K. J. Noone, L. M. Russell and J. P. Putaud, 2000: In situ aerosol –size distributions and clear-column radiative closure during ACE-2. *Tellus*, **52B**, 498-525.
- Durkee, P. A., F. Pfeil, E. Frost, and R. Shema, 1991: Global analysis of aerosol particle characteristics. *Atmos. Env.*, **25A**, 2457-2471.
- Durkee, P. A., K. E. Nielsen, P. J. Smith, P. B. Russell, B. Schmid, J. M. Livingston, B. N. Holben, C. Tomasi, V. Vitale, D. Collins, R. C. Flagan, J. H. Seinfeld, K. J. Noone, E. Öström, S. Gasso, D. Hegg, L. M. Russell, T. S. Bates and P. K. Quinn, 2000: Regional aerosol optical depth characteristics from satellite observations: ACE-1, TARFOX and ACE-2 results. *Tellus*, **52B**, 484-497.
- Higurashi, A. and T. Nakajima, 1999: Development of a two channel aerosol retrieval algorithm on global scale using NOAA/AVHRR. *J. Atmos. Sci.*, **56**, 924-941.
- Higurashi, A. T., T. Nakajima, B. N. Holben, A. Smirnov, R. Frouin, and B. Chateret, 1999: A study of global aerosol optical climatology with two channel AVHRR remote sensing. *J. Climate*, **13**, 2011-2027.
- Holben, B. N., T. F. Eck, I. Slutsker, D. Tanré, J. P. Buis, A. Setzer, E. Vermote, J. A. Reagan, Y. J. Kaufman, T. Nakajima, F. Lavenu, I. Jankowiak, and A. Smirnov, 1998: AERONET – A federated instrument network and data archive for aerosol characterization. *Remote Sens. Environ.*, **66**, 1-16.
- Huebert, B., T. Bates, P. Russell, G. Shi, Y. J. Kim, and K. Kawamura, 2003: An overview of ACE-Asia: strategies for quantifying the relationships between Asian aerosols and their climatic impacts. *J. Geophys. Res.* (*in press*).
- Intergovernmental Panel on Climate Change (IPCC), 1996. Climate Change 1995, J. T. Houghton *et al.* (Eds.). Cambridge University Press, New York.

- Kauffman, Y. J., D. Tanré, O. Dubovik, A. Karnieli, and L. A. Remer, 2001: Absorption of sunlight by dust as inferred from satellite and ground-based remote sensing. *Geophys. Res. Lett.*, **24**, 1479-1482.
- King, M. D., Y. J. Kaufman, D. Tanré, and T. Nakajima, 1999: Remote sensing of tropospheric aerosols from space: past, present and future. *Bull. Am. Meteor. Soc.*, **80**, 2229-2259.
- Kuciauskas, A. P., 2002: Aerosol optical depth analysis with NOAA GOES and POES in the western Atlantic. M.S. Thesis, Naval Postgraduate School, Monterey, CA, 81 pp.
- Maring, H., D. L. Savoie, M. A. Izaguirre, C. McCormick, R. Arimoto, J. M. Prospero, and C. Pilinis, 2000: Aerosol physical and optical properties and their relationship to aerosol composition in the free troposphere at Izana, Tenerife, Canary Islands, during July 1995, *J. Geophys. Res.*, **105**, 14677-14700.
- Mischenko, M. I., L. D. Travis, R. A. Kahn, and R. A. West, 1997: Modeling phase functions for dust-like tropospheric aerosols using a shape mixture of randomly oriented polydisperse spheroids, *J. Geophys. Res.*, **102**, 16831-16847.
- Prospero, J.M., 1999: Long-term measurements of the transport of African mineral dust to the southeastern United States: Implications for regional air quality. *J. Geophys. Res.*, **104**, 15917-15927.
- Rao, C. R. N. and J. Chen, 1995: Inter-satellite calibration linkages for the visible channels of the Advanced Very High Resolution Radiometer on the NOAA-7, -9, and -11. *Int. J. Rem. Sen.*, **16**, 1931-1942.
- Rao, C. R. N. and N. Zhang, 1999: Calibration of the visible channel of the GOES images using the Advanced Very High Resolution Radiometer. Pre-print volume, 10th Atmospheric Radiation Conference (Madison, Wisconsin), 560-563.
- Rao, C. R. N., C. J. Sullivan, and N. Zhang, 1999: Post-launch calibration of meteorological satellite sensors. *Adv Space Res.*, **23**, 1357-1365.
- Reid, J. S., J. E. Kinney, D. L. Westphal, B. N. Holben, E. J. Welton, S. Tsay, D. P. Eleuterio, J. R. Campbell, S. A. Christopher, P. R. Colarco, H. H. Jonsson, J. M. Livingston, H. B. Maring, M. L. Meier, P. Pilewskie, J. M. Prospero, E. A. Reid, L. A. Remer, P. B. Russell, D. L. Savoie, A. Smirnov, and D. Tanré, 2003: Analysis of measurements of Saharan dust by airborne and ground-based remote sensing methods during the Puerto Rico Dust Experiment (PRIDE), *J. Geophys. Res.* (in press).
- Smith, P. J., 1998: Remote measurement of aerosol optical properties using the NOAA POES AVHRR during ACE-1, TARFOX, and ACE-2. M.S. Thesis, Naval Postgraduate School, Monterey, CA, 58 pp.

Turner, R., 1973: Atmospheric effects in remote sensing. In *Remote Sensing of the Earth Resources, II*, 549-583, F. Shahrocki (ed.), University of Tennessee.

Twomey, S., M. Piepgrass and T. L. Wolfe, 1977: An assessment of the impact of pollution on global cloud albedo. *Tellus*, **36B**, 356-366.

Westphal, D. L., 2003: Real-time applications of a global multicomponent aerosol model, *J. Geophys. Res.*, in press, 2003.

**Table 1. NOAA AVHRR Radiometric Channels.**

<b>Channel</b>	<b>Band Widths (<math>\mu\text{m}</math>)</b>
1 (visible)	0.58 – 0.68
2 (Near Infrared)	0.725 – 1.10
3 (infrared)	3.55 – 3.93
4 (infrared)	10.3 – 11.3
5 (infrared)	11.5 – 12.5

**Table 2. GOES Imager Radiometric Channels.**

<b>Channel</b>	<b>Band Widths (<math>\mu\text{m}</math>)</b>
1 (Visible)	0.55 – 0.75
2 (infrared)	3.80 – 4.00
3 (infrared)	6.50 – 7.00
4 (infrared)	10.20 – 11.20
5 (infrared)	11.50 – 12.50

**Table 3.** List of 22 cases that include the GOES and NOAA pass times (in UTC) and locations. The case studies are identified in sequential numbers, shown in parentheses.

Dates	Satellite Times	Study locations
27 July	GOES-8: 16:45 –21:15, NOAA-16: 18:42, NOAA-14: 21:51, NOAA-14: 21:51	Guadeloupe Isl
28 July	GOES-8: 17:15 – 21:15, NOAA-16:18:31, NOAA –14 :21:39	La Paguera
02 Sept	GOES-8: 17:15 – 21:15, NOAA-16: 17:18, NOAA-14: 21:08	Bermuda
04 Sept	GOES-8: 16:45 – 21:15, NOAA-16: 18:35	Guadeloupe Isl.
05 Sept	GOES-8: 17:15 – 21:15, NOAA-16: 18:26	La Paguera
06 Sept	GOES-8: 17:15 – 21:15, NOAA-16: 18:16	Guadeloupe Isl.
07 Sept	GOES-8: 17:15 – 21:15, NOAA-16: 18:05	Guadeloupe Isl.
08 Sept	GOES-8: 17:15 – 21:15, NOAA-16: 17:55	Guadeloupe Isl.
11 Sept	GOES-8: 15:15 – 20:45, NOAA-14: 21:00	Bermuda
11 Sept	GOES-8: 15:15 – 20:45, NOAA-14: 21:00	Guadeloupe Isl.
17 Sept	GOES-8: 16:15 – 20:45, NOAA-16: 18:01	Bermuda
17 Sept	GOES-8: 16:15 – 20:45, NOAA-16: 18:01	Guadeloupe Isl.
18 Sept	GOES-8: 16:45 – 21:15, NOAA-16: 17:50, NOAA-14: 21:16	Bermuda
18 Sept	GOES-8: 16:45 – 20:45, NOAA-16:17:50, NOAA-14: 21 :16	Guadeloupe Isl.
19 Sept	GOES-8: 15:15 – 21:15, NOAA-16: 17:40, NOAA-14: 21:04	Bermuda
19 Sept	GOES-8: 15:15 – 18:45, NOAA-16: 17:40	La Paguera
20 Sept	GOES-8: 14:45 – 21:15, NOAA-16: 17:29, NOAA-14: 20:53	Bermuda
21 Sept	GOES-8: 14:15 – 21:15, NOAA-16: 17:19, NOAA-16: 19:00	La Paguera
22 Sept	GOES-8: 14:15 – 21:15, NOAA-16: 18:47	La Paguera
23 Sept	GOES-8: 17:15 – 21:15, NOAA-16: 18:38	La Paguera
25 Sept	GOES-8: 13:15 – 20:45, NOAA-16: 18:17	Bermuda
29 Sept	GOES-8: 13:15 – 21:15, NOAA-16: 17:35	La Paguera

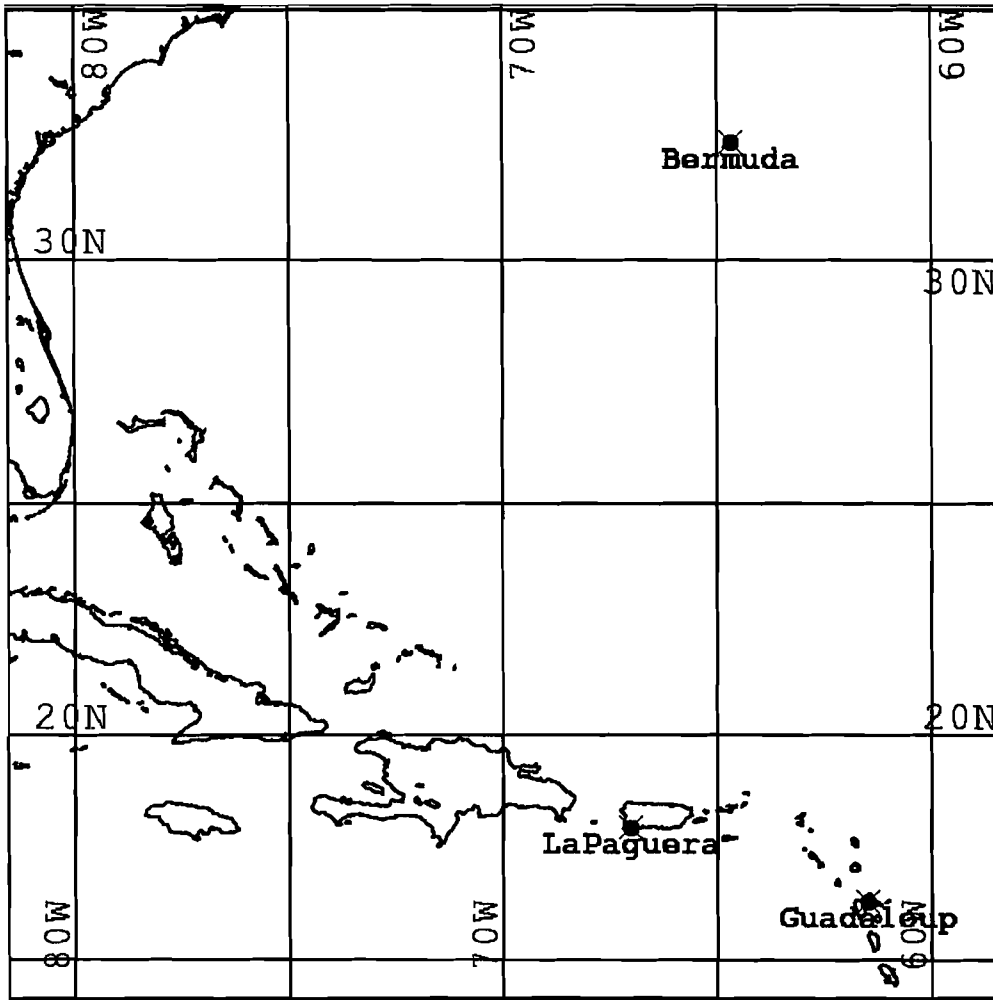


**Figure 1.** Map of the experimental region with locations of the AERONET stations.

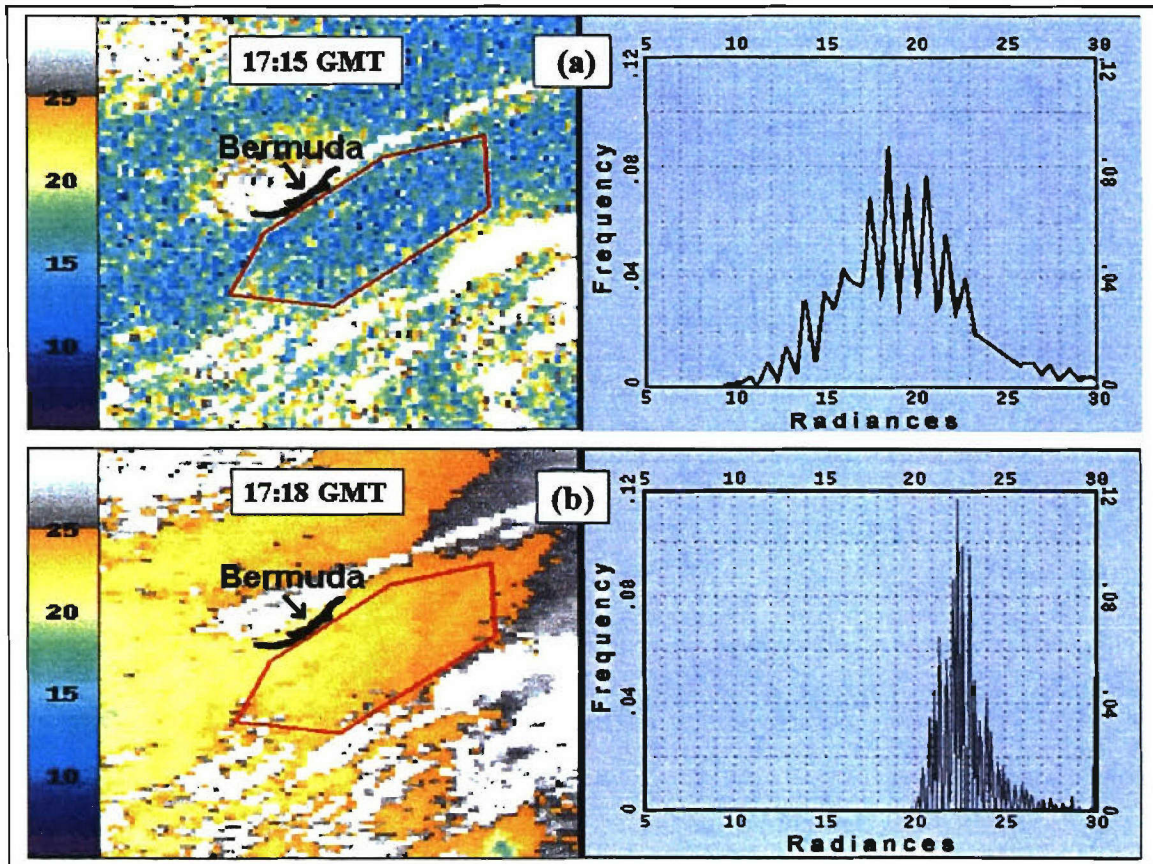


**Figure 2.** Comparisons of radiance images and associated frequency of radiance histograms between (a) GOES-8 and (b) NOAA-16 on 02 September 2001. Histograms were developed from areas within red annotations. Radiances, as shown within the color legend and the histogram x axis, are in units of  $\text{Wm}^{-2}\text{sr}^{-1}\mu\text{m}^{-1}$ .

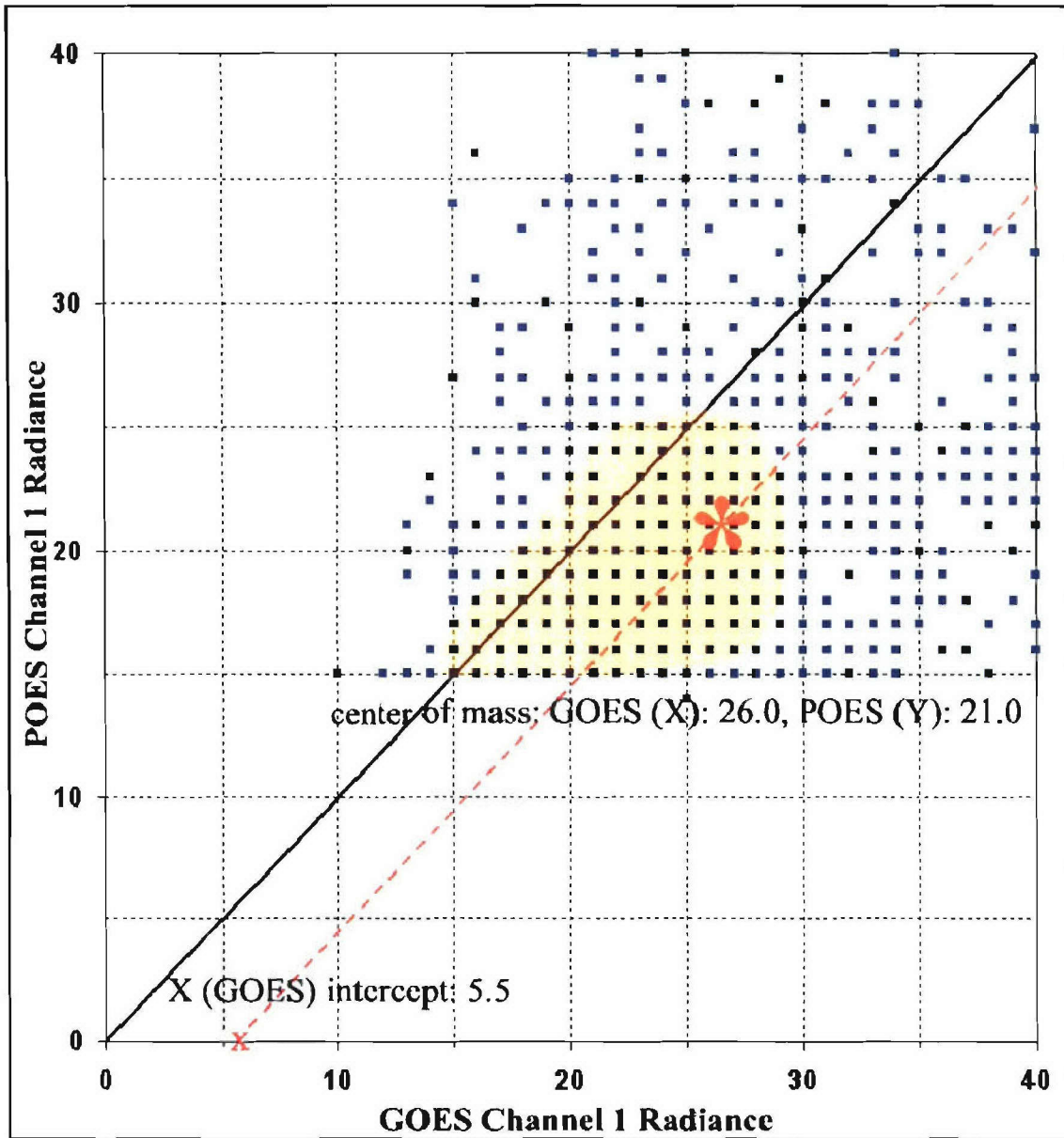


**Figure 3.** Comparisons of Channel 1 radiances between GOES-8 and NOAA-16. Radiances are in units of  $\text{Wm}^{-2}\text{sr}^{-1}\mu\text{m}^{-1}$ . Orange shade indicates region of high density of multiple occurrences. Black solid line represents one to one relationship and red dashed line represents 'best-fit' relationship between GOES and POES. Red asterisk represents center of mass point within the data.

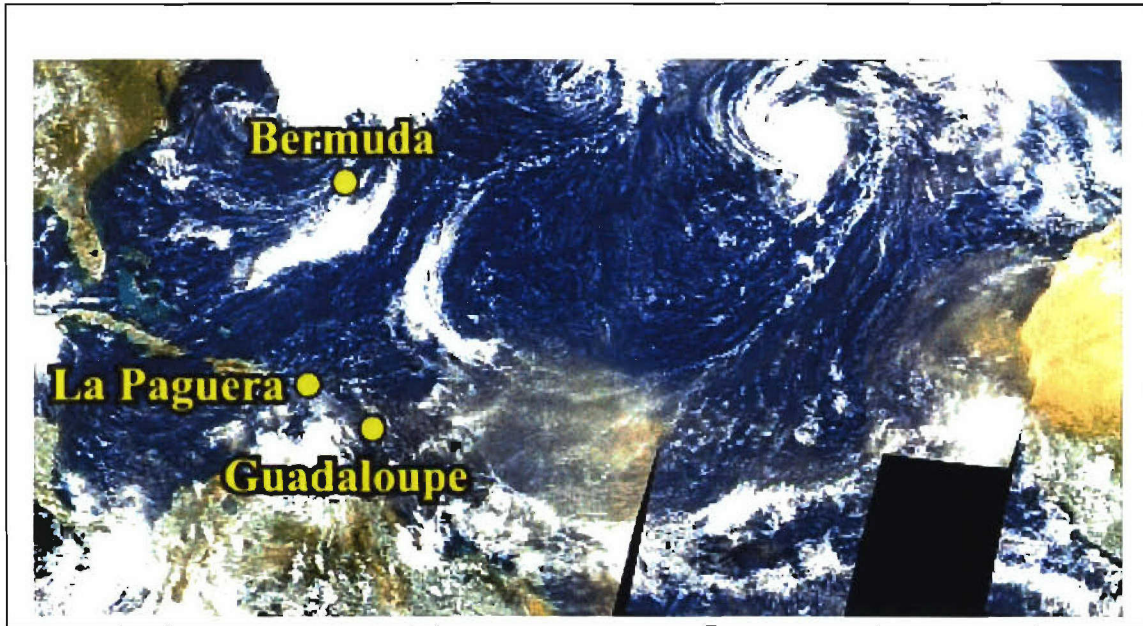


**Figure 4.** Composite of SeaWiFS images centered at 12 UTC on 17 September 2001 covering the Atlantic Basin. Over the ocean, clear (low aerosol content) regions are in dark blue, cloudy regions are solid white, and gray-yellow regions depict higher aerosol (dust) content. The annotations represent the locations of AERONET sites used for this study. (Image provided by the SeaWiFS Project, NASA/Goddard Space Flight Center, and ORBIMAGE)

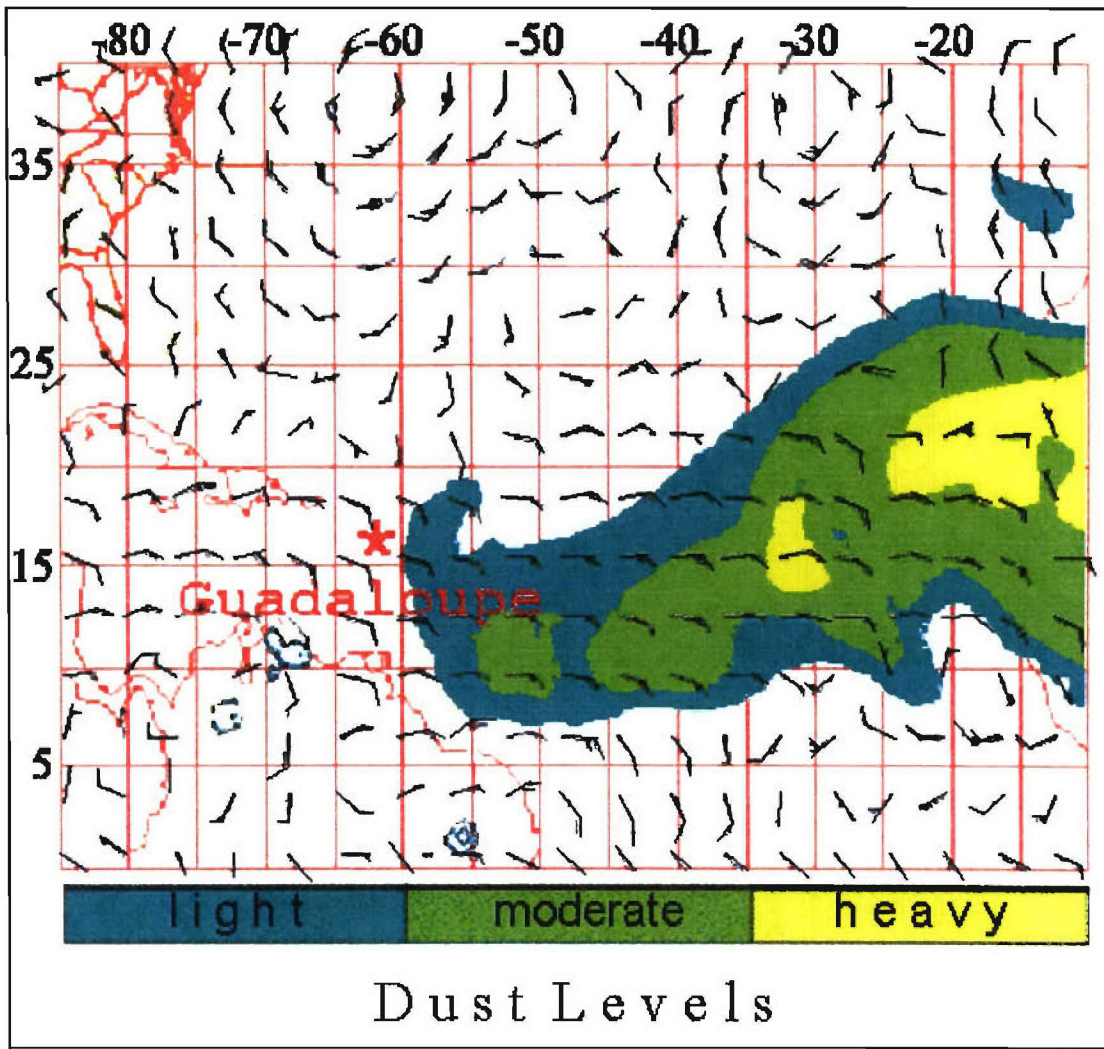


**Figure 5.** NAAPS display of significant dust levels and 850 mb winds from NOGAPS over the Atlantic Ocean basin for 18 September 2001, 18:00 UTC. (Courtesy of Dr. Douglas L. Westphal at NRL)

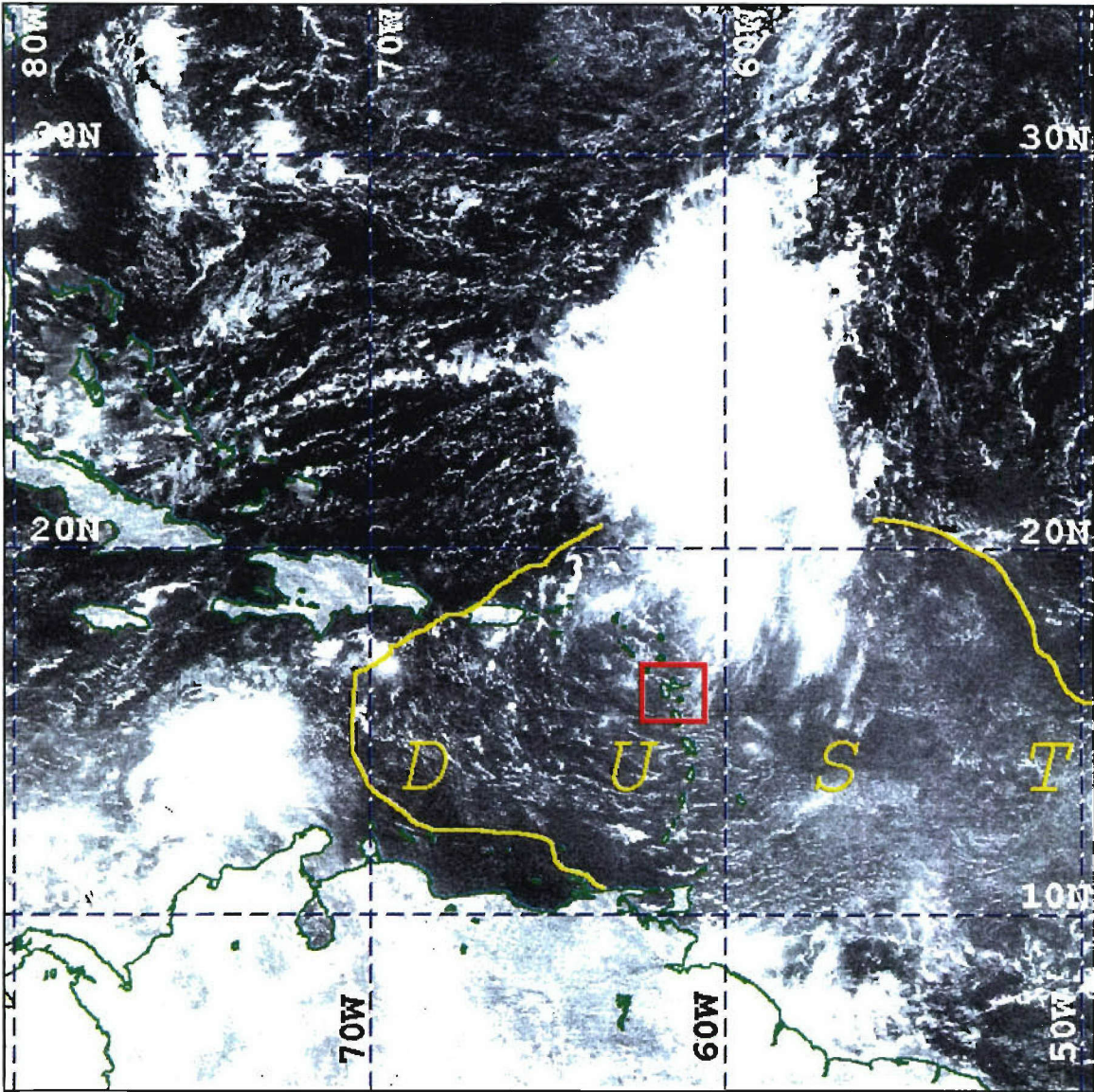


**Figure 6.** GOES-8 visible image for 18 September 2000 at 17:15 UTC. The annotated box surrounds the region of Guadeloupe Island. The area of dust aerosol is also annotated.

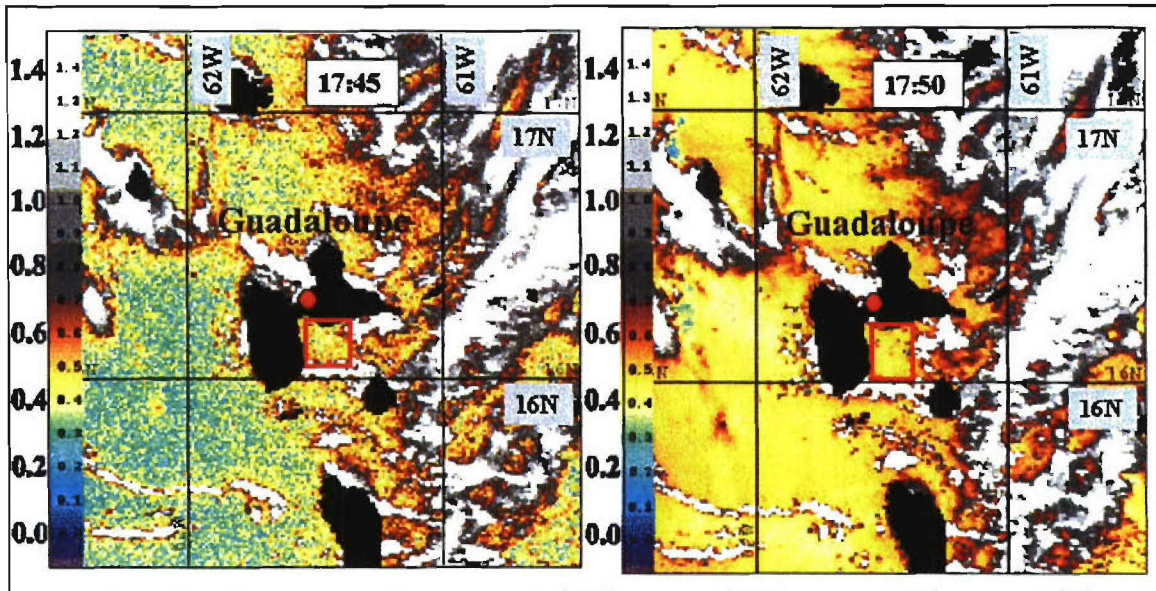


**Figure 7.** AOD images generated for 18 September 2001 at 17:45 UTC and 17:50 UTC from GOES-8 and NOAA-16 data, respectively. Images surround Guadeloupe Island (outlined in black). Clouds are gray/white shades. Pixel sizes are 1.1 km by 1.1 km and the domain is approximately 110 km by 110 km. Red boxes depict the locations where the representative AOD for that area were measured. AOD color contours are defined on the left side of each image.

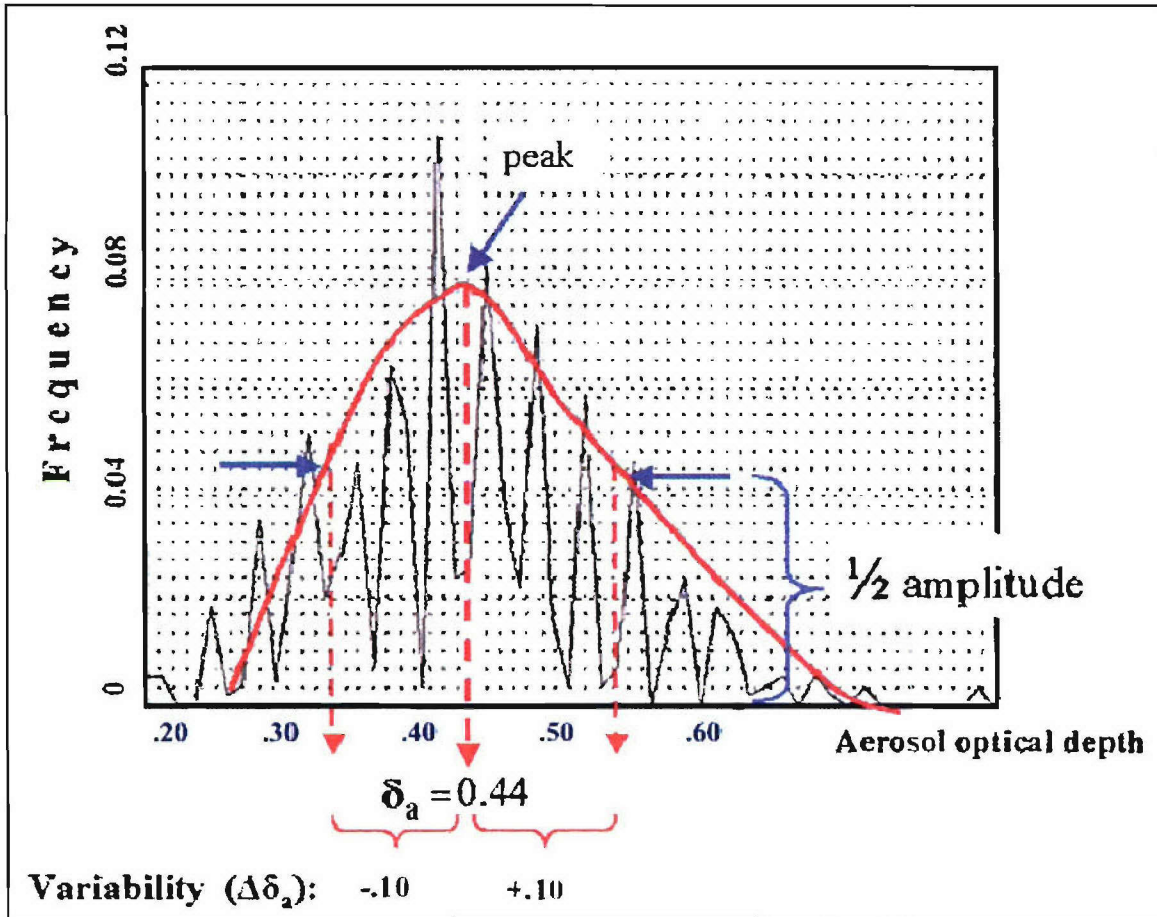


**Figure 8.** Histogram frequency plot of AOD obtained from within the annotated red box in Figure 7, 17:45 UTC image. Red annotations indicate methods of extracting AOD and the associated measurement variability. The analyzed distribution is manually drawn by a solid red curve. The peak of the AOD distribution translates to an AOD estimate of 0.44. Variability estimates of AOD are obtained at half of the amplitude of the red curve on either side of the estimated AOD.

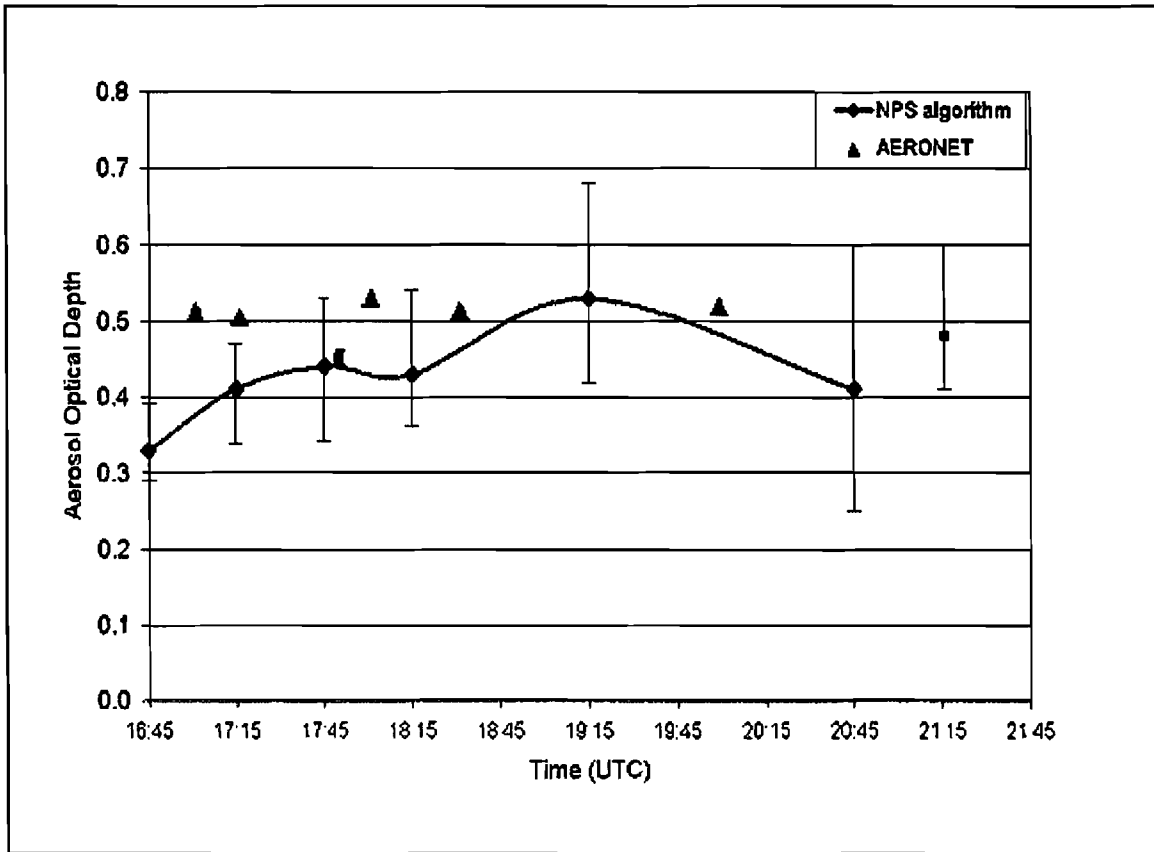


**Figure 9.** Chart of satellite-derived AOD (navy blue dots) and AERONET AOD (green) for 18 September 2001 over Guadalupe Island. NOAA data are presented as individual blue squares whereas GOES-8 data are blue diamonds connected with a blue line. Red bars represent variability estimates in AOD measurements.

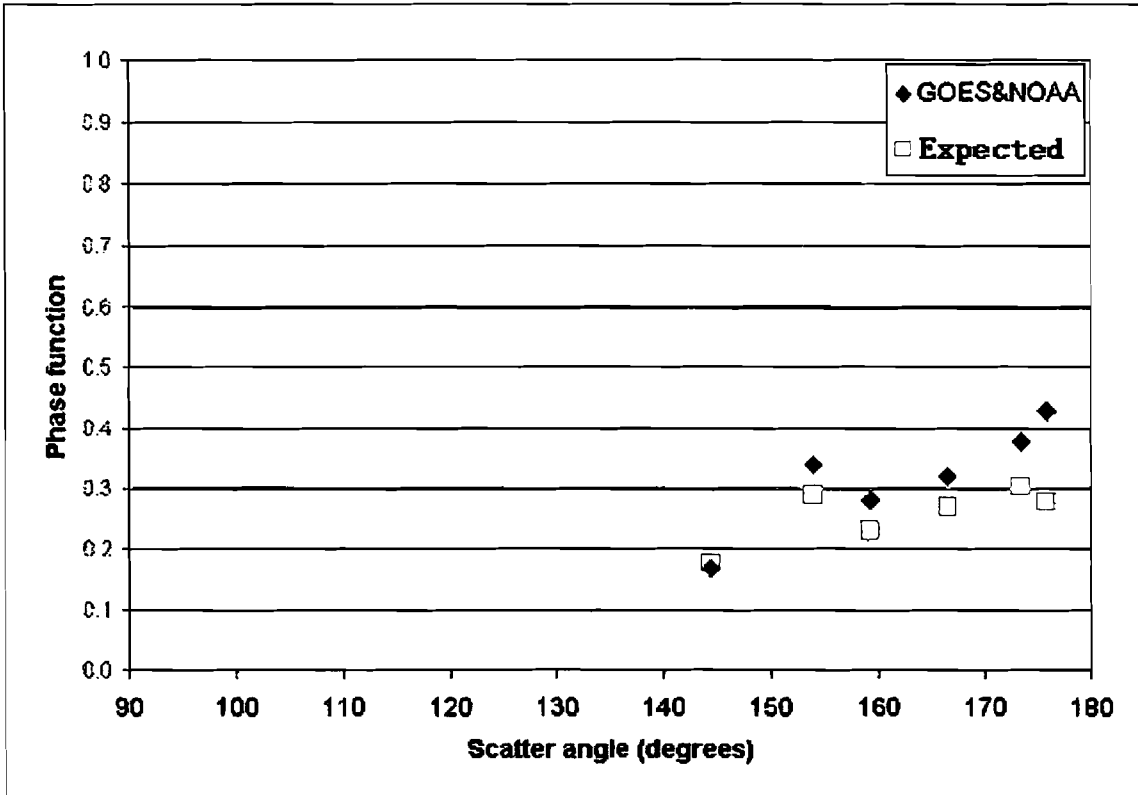


**Figure 10.** Plot of phase function as a function of scatter angle for the case of 18 September 2001 over Guadalupe Island. Blue diamonds indicate phase functions inferred by the NPS algorithm based on the satellite data. Red boxes indicate the phase function values required for the satellite-derived AOD to match AERONET AOD.

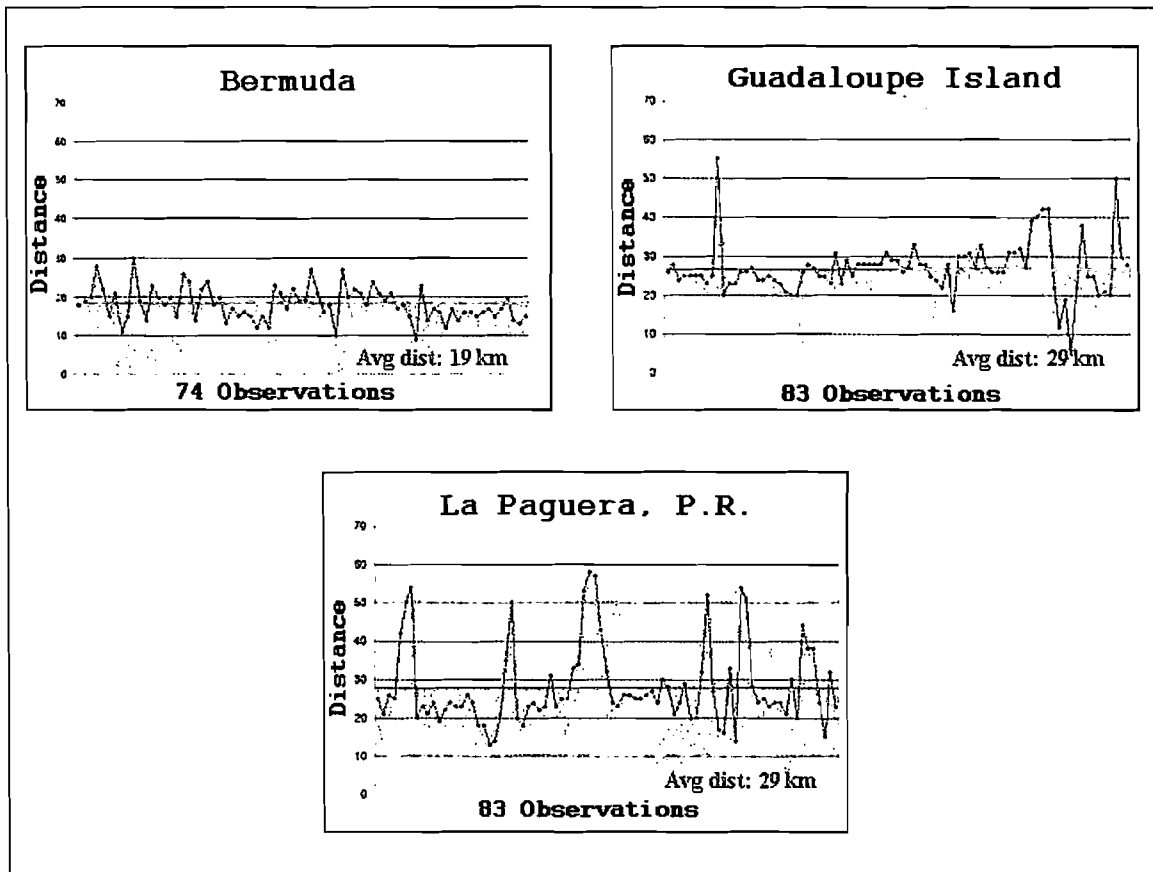


**Figure 11.** Distribution of distance measurements between each of the 3 AERONET sites and the location of the satellite-derived AOD for all 22 cases. For each AERONET region, the average distance from the AERONET station to the center of the satellite-derived measurement box is annotated in red.

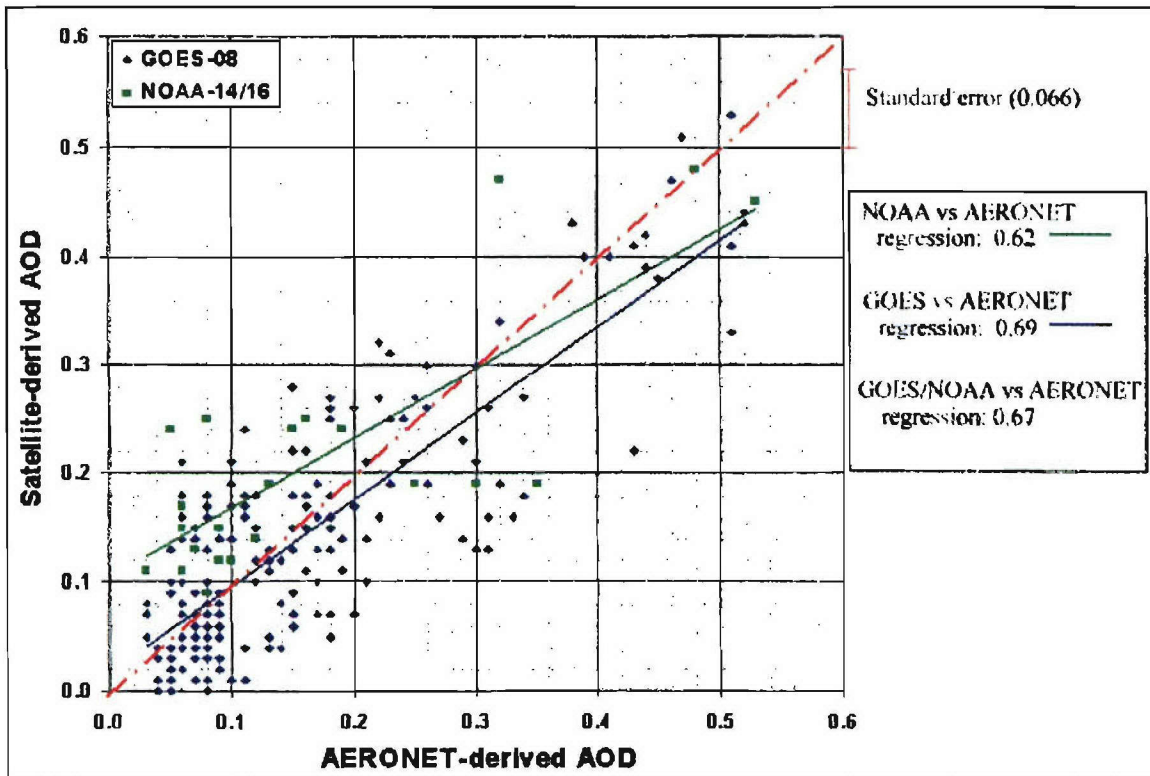


**Figure 12.** Comparisons between NPS-calculated AOD and AERONET-observations of AOD for the 22 cases as listed in Table 3. The dashed red line depicts one to one relationship. The blue and green lines represent the ‘best fit’ curves for the GOES and NOAA-POES satellites, respectively.

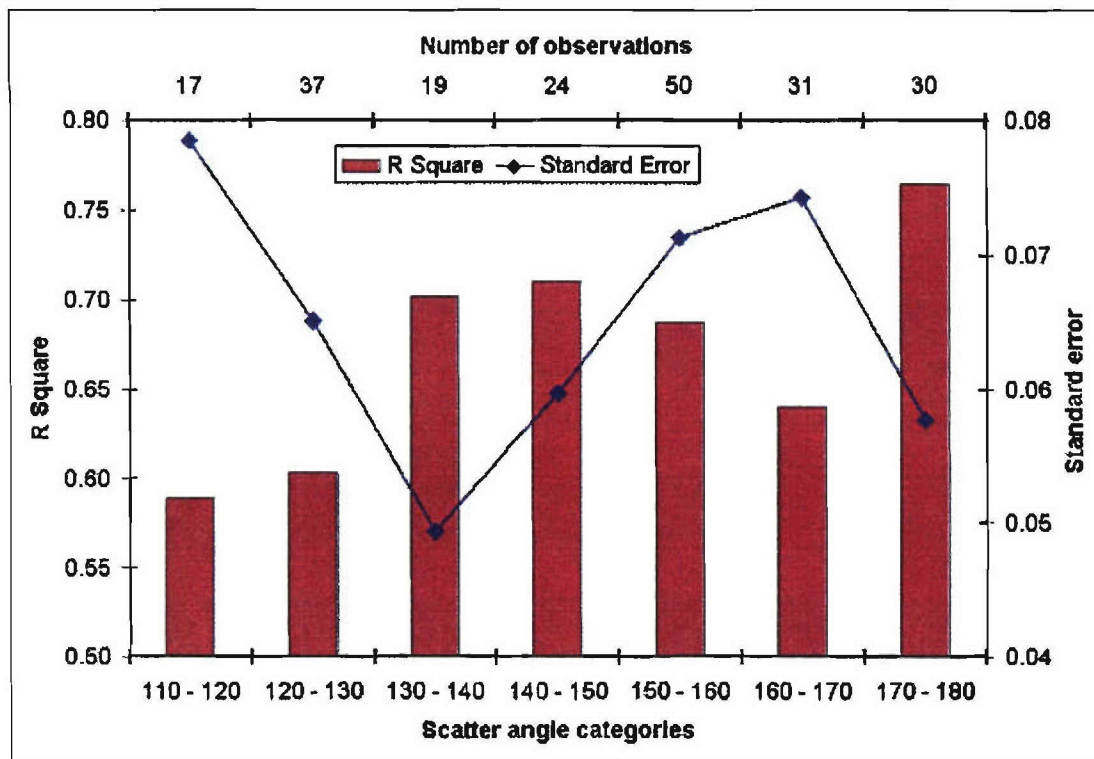


Figure 13. Evaluation of NPS algorithm, partitioned over categories of scatter angles.

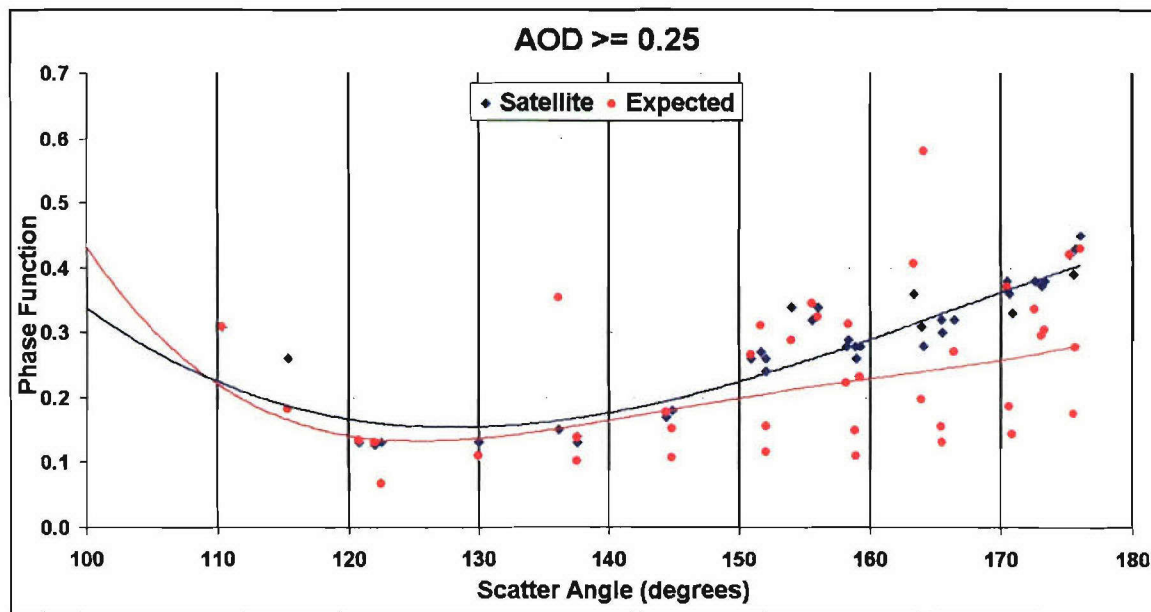
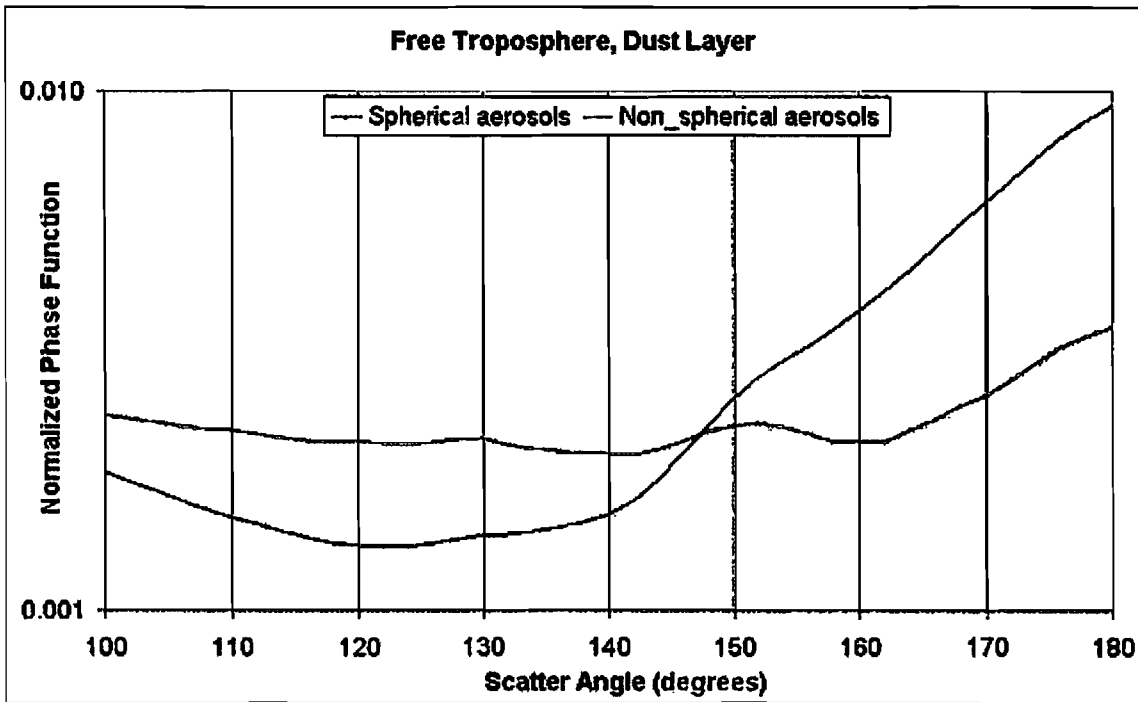
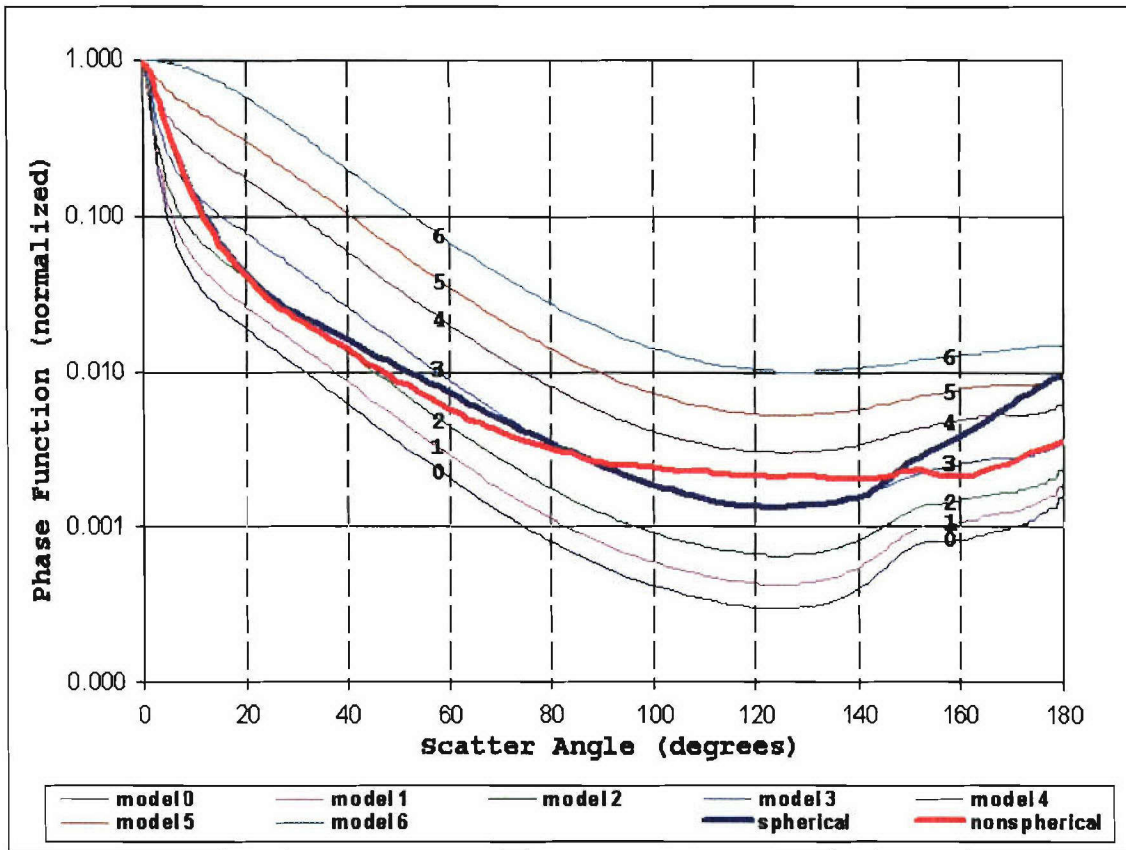


Figure 14. Comparisons of phase functions between satellite data (blue diamonds) and AERONET data (red circles) for 22 cases. Associated 'best-fit' curves were generated by applying a 4<sup>th</sup> order polynomial. Figure only depicts dust conditions (AERONET AOD  $\geq 0.25$ ).



**Figure 15.** Phase function plots for the free troposphere, dust layer obtained from the second Aerosol Characterization Experiment (ACE-2). Data is supplied by Collins, *et al.* (2000). Phase function values are normalized.



**Figure 16.** Phase function plots comparing the dust plots in Collins *et al.* (2000) (thick curves) with the model phase functions used in the NPS algorithm (thin curves). Annotated numbers are used to identify the model numbers.